metals

Article

Structural Stability Analysis of Eye of the Yellow Sea, a Large-Span Arched Pedestrian Bridge

Zhihua Chen [1,2], Hao Lin [1], Xiaodun Wang [1,2,*], Hongbo Liu [2,3,*], Ken'ichi Kawaguchi [4] and Minoru Matsui [5]

1 Department of Civil Engineering, Tianjin University, Tianjin 300072, China; zhchen@tju.edu.cn (Z.C.); lhao001@126.com (H.L.)
2 State Key Laboratory of Hydraulic Engineering Simulation and Safety, Tianjin University, Tianjin 300072, China
3 Department of Civil Engineering, Hebei University of Engineering, Handan 056000, China
4 Institute of Industrial Science, The University of Tokyo, Tokyo 153-8505, Japan; kawaken@iis.u-tokyo.ac.jp
5 Kawaguchi & Engineers Co., Ltd., Tokyo 102-0071, Japan; matui_m@kawa-struc.com
* Correspondence: maodun2004@126.com (X.W.); hb_liu2008@163.com (H.L.)

Abstract: To date, scholars' research on the stability behavior of the arch structure mainly focuses on solid–web section arches, steel tubular truss arches and concrete-filled steel tubular arches, but the stability behavior of the novel spatial grid arch structure, which integrates the characteristics of grid structure and arch structure, is not yet clear. Based on the Eye of the Yellow Sea pedestrian bridge project in Rizhao, China, the stability behavior of this large-span spatial grid arch structure was studied, in this paper, by the project's structure design team. The project is a glass covered steel arch pedestrian bridge with a span of 177 m, a height of 63.5 m, an elliptical section with a long axis of 18 m, and a short axis of 13.5 m. The elastic and the nonlinear elasto-plastic stability behavior considering different initial geometric imperfections, was analyzed by the ABAQUS finite element model. The buckling modes and the full-range load-displacement curve of the structure were analyzed, and the stress distribution, deformation mode and overall structural performance during the whole loading process were analyzed. The effects of initial imperfections, geometric nonlinearity and material nonlinearity on the ultimate load-carrying capacity of the structure were studied. The stability behavior of large-span spatial grid arch structure was studied in this paper, which provides an important reference for the design and analysis of such structures.

Keywords: arch structure; stability behavior; spatial grid arch structure; stability analysis; initial imperfections; nonlinear factors; ultimate load-carrying capacity

Citation: Chen, Z.; Lin, H.; Wang, X.; Liu, H.; Kawaguchi, K.; Matsui, M. Structural Stability Analysis of Eye of the Yellow Sea, a Large-Span Arched Pedestrian Bridge. *Metals* **2022**, *12*, 1138. https://doi.org/10.3390/met12071138

Academic Editor: Ulrich Prahl

Received: 9 May 2022
Accepted: 2 July 2022
Published: 3 July 2022

1. Introduction

The arch structure is one of many structural systems, and has a wide range of applications in building and bridge projects. To date, a large amount of research has been conducted on the stability behavior of traditional arch structures commonly used in engineering. By using an analytical method, Timoshenko [1] derived the equation of the in-plane buckling load from the equilibrium differential equation of the pin-ended arch under uniform compression, which laid the foundation for the theory of the in-plane stability of the arch. Pi and Bradford [2–9] studied the in-plane nonlinear elastic stability behavior of circular arches with boundary conditions of hinged, fixed, one hinged and one fixed, and unequal rotational restraints under a centrally concentrated load. Hodges [10] studied the nonlinear in-plane deformation and bucking of rings and high arches under a hydrostatic pressure effect. Sakimoto and Namita [11] investigated the out-of-plane buckling of solid rib arches braced with transverse bars. By using the principal of stationary potential energy and Rayleigh–Ritz method, Pi and Bradford [12–23] proposed analytical solutions for the elastic bending and torsional buckling loads of circular arches with boundary conditions of hinged, fixed and in-plane elastic rotation constraints under concentrated forces, uniform compression and uniform bending. Dou et al. [24] first proposed a method for solving the shear and torsional stiffness of truss arches, and derived an analytical solution for the buckling load of lateral bending and torsional instability of truss arches with fixed restraints under uniform compression and bending based on the energy method. Guo et al. [25,26] derived elastic support stiffness thresholds for the out-of-plane instability of truss arches and solid web arches with lateral discrete bracing. By using the finite element method, Komatsu and Sakimoto [27,28] studied the out-of-plane elasto-plastic buckling load of a box cross-sectional arch with rise-to-span ratios of 0.1 to 0.2 under a uniform load. Pi et al. [29–31] studied the out-of-plane elasto-plastic bending–torsional buckling and post-buckling behavior of H-section steel arches under various loads, introducing the regularized slenderness ratio and the stability coefficients of axial compression columns or pure bending beams into the Australian code, and proposed formulas for calculating the out-of-plane elastic load-carrying capacity of uniformly compressed arches and uniformly bent arches. Dou et al. [32] investigated flexural–torsional buckling and ultimate resistance of parabolic steel arches subjected to a uniformly distributed vertical load. Dou et al. [33] conducted static stability tests of three groups of circular arches with the same span but different rise-to-span ratios, and the out-of-plane load-carrying capacity of the arch under 3-point symmetric and 2-point asymmetric loading was investigated. The stability behavior of the novel large-span spatial grid arch structure applied to the Eye of the Yellow Sea pedestrian bridge has not yet been studied.

1.1. Project Overview

The Eye of the Yellow Sea, which is a glass-covered steel arched pedestrian bridge with a span of 177 m, a height of 63.5 m, an elliptical section with a long axis of 18 m, and a short axis of 13.5 m, is located over an estuary in Rizhao, China. The highest part of the bridge is equipped with a semicircular viewing platform extending to both sides, with a radius of 9 m and an area of 398 square meters.

1.2. Structure Information

In order to satisfy the experience of visitors passing inside the arch, and the features of open eyesight and good perspective, a novel spatial grid arch structure was applied to the Eye of the Yellow Sea large-span arched pedestrian bridge. The structure integrates the characteristics of grid structure and arch structure, consisting of arch components, ring components and bracing components, with a grid size of about 4.5 m × 4.5 m. The basic cross section of the structure is an ellipse with a long axis of 18 m and a short axis of 13.5 m. The overall structure model is shown in Figure 1.

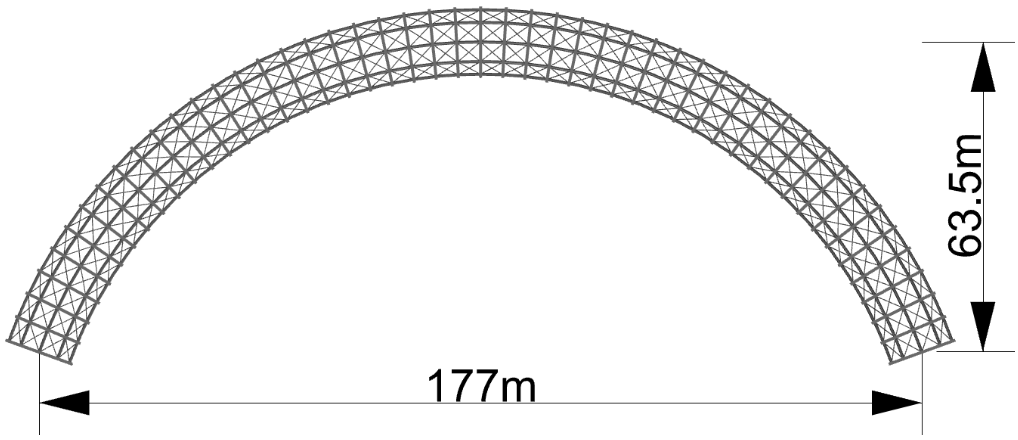

Figure 1. Overall structure model diagram.

As shown in Figure 2, the structure uses circular steel tubes for the arch components, H-shaped steel for the ring components, and steel tie rods for the bracing components.

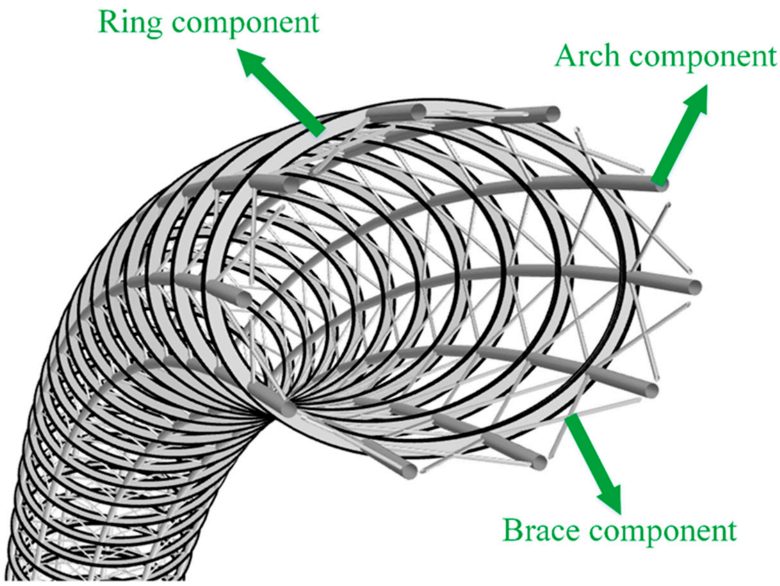

Figure 2. Basic cross section of the structure.

2. Finite Element Mode

According to the Eye of the Yellow Sea pedestrian bridge project, the structure model is divided into eight areas according to the different sizes of components' sections, and divided into three load regions according to the value of the vertical loads. Based on the above partition, the finite element model was established in ABAQUS. As shown in Figure 3, the component section partition and load partition are illustrated with the half structure.

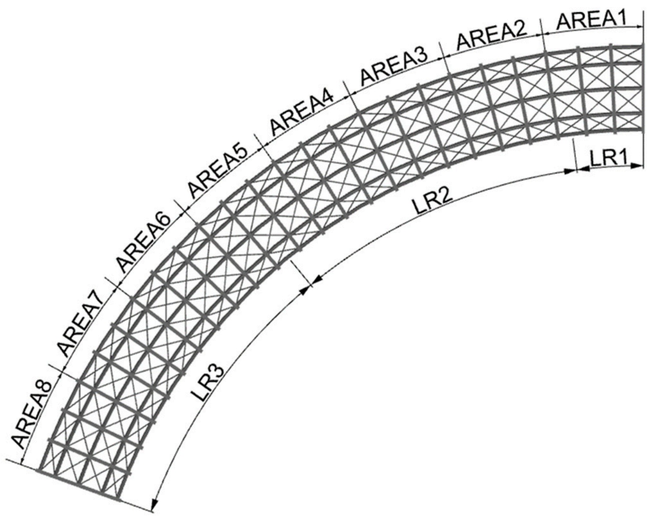

Figure 3. Regional division of the structure. Load region is notated as LR in the figure.

In the finite element model, the B31 element was used for the simulation of the ring and arch components, and the T3D2 truss element was used for the simulation of the bracing component, and were defined as tensile-only elements. The material's elastic modulus was set as 2.06×10^{11} Pa, Poisson's ratio as 0.3, density as 7.85×10^{3} kg/m^3, yield strength as 345 MPa, and the material was considered as ideal elasto-plastic. The materials and major cross section sizes of the ring components, arch components and bracing components for the different areas are listed in Table 1.

Table 1. Summary of component information.

AREA	AREA1	AREA2	AREA3	AREA4	AREA5	AREA6	AREA7	AREA8
Ring (mm) Q345	B.Pipe-600 × 28	B.Pipe-600 × 28	B.Pipe-600 × 26	B.Pipe-600 × 26	B.Pipe-600 × 26	B.Pipe-600 × 26	B.Pipe-600 × 40	B.Pipe-600 × 40
Arch (mm) Q345	BH-700 × 300 × 22 × 22	BH-700 × 300 × 22 × 22	BH-700 × 300 × 20 × 20	BH-700 × 300 × 20 × 20	BH-700 × 300 × 20 × 20	BH-700 × 300 × 20 × 20	BH-700 × 300 × 36 × 22	BH-700 × 300 × 36 × 22
Brace (mm) Q460	Rod Φ185	Rod Φ185	Rod Φ185	Rod Φ185	Rod Φ185	Rod Φ185	Rod Φ185	Rod Φ185

According to the actual engineering situation, the dead loads (including 3 kN/m^2 for platform, deck and stairs, 9 kN/m^2 for escalator, and 10 kN/m^2 for elevator), and live loads (including 3.5 kN/m^2 for platform, deck and stairs, and 0.5 kN/m^2 for roof maintenance), were counted separately by different load regions, converted into nodal loads for each region, and added to the finite element model. The loads' direction was vertically downward, and the acceleration of gravity was 9.8 m/s^2. Model loads are shown as Figure 4.

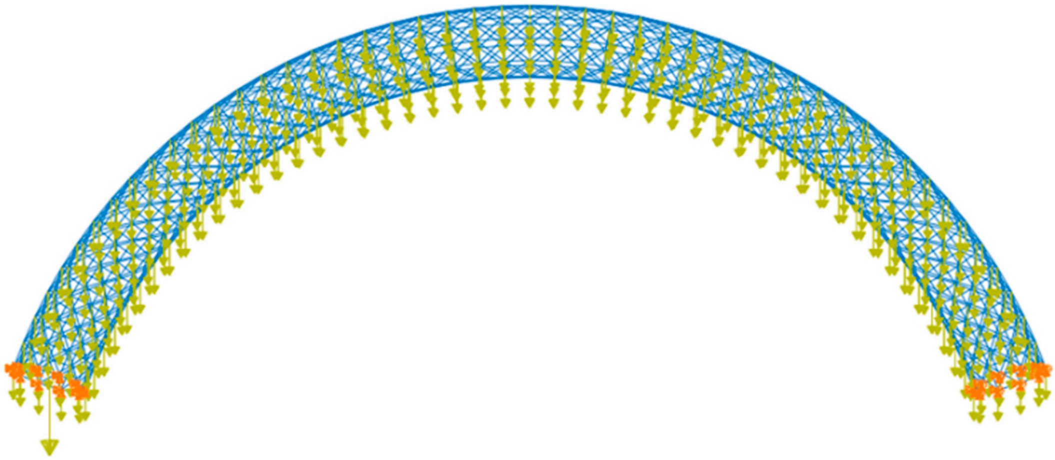

Figure 4. Nodal loads and gravity load in the finite element model.

The Merge function was used in the finite element model to create the welded connection between the components, the MPC Pin was used to simulate the hinge joint constraint, and the hinged constraint was set at the end of each arch component at the arch feet, as shown in Figure 5.

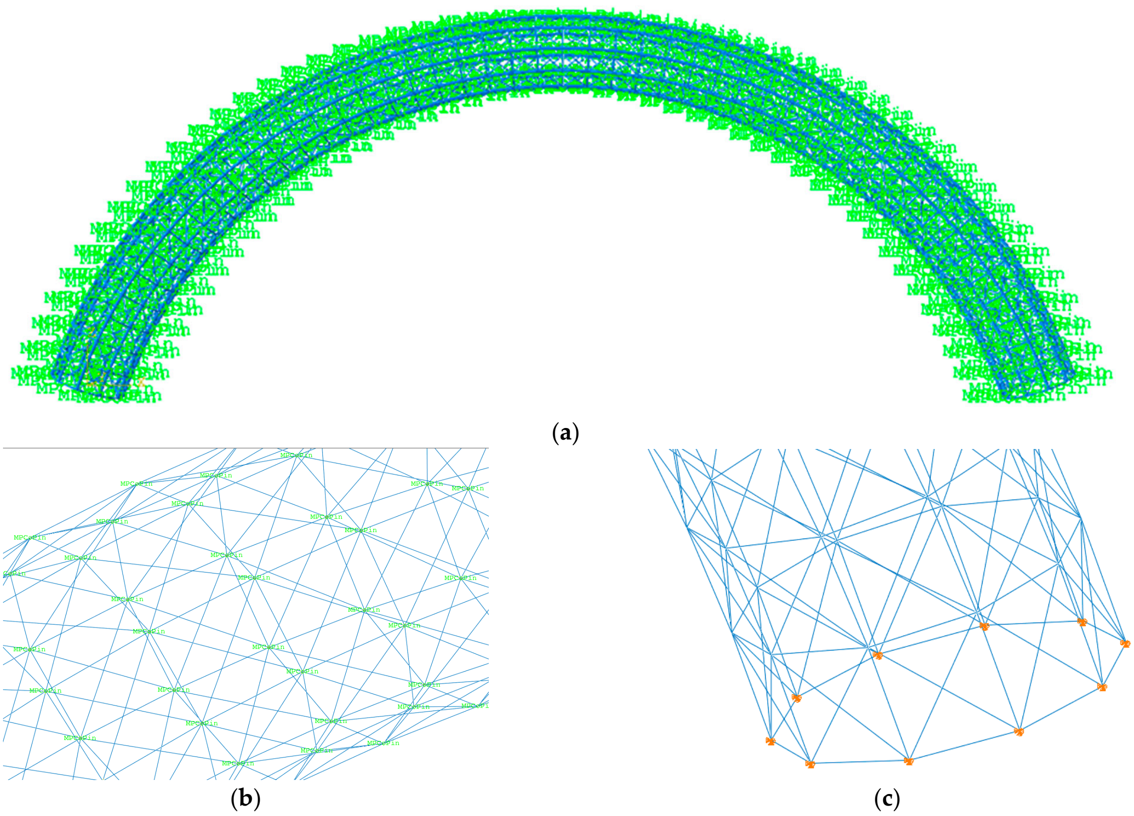

Figure 5. Finite element model constraint information: (**a**) Overview; (**b**) MPC Pin; (**c**) Hinged constraint.

3. Stability Behavior Analysis

3.1. Linear Buckling Analysis

Through linear buckling analysis, the elastic buckling load of the structure and the corresponding buckling modes was obtained to determine the weak regions of the structure. At the same time, consistent initial geometric imperfections were applied to the structure according to the buckling modes, which were used as the basis for the nonlinear elasto-plastic stability analysis of the structure [34]. The first six buckling modes of the structure under "1.0Dead Load + 1.0Live Load" load combination are shown in Figure 6.

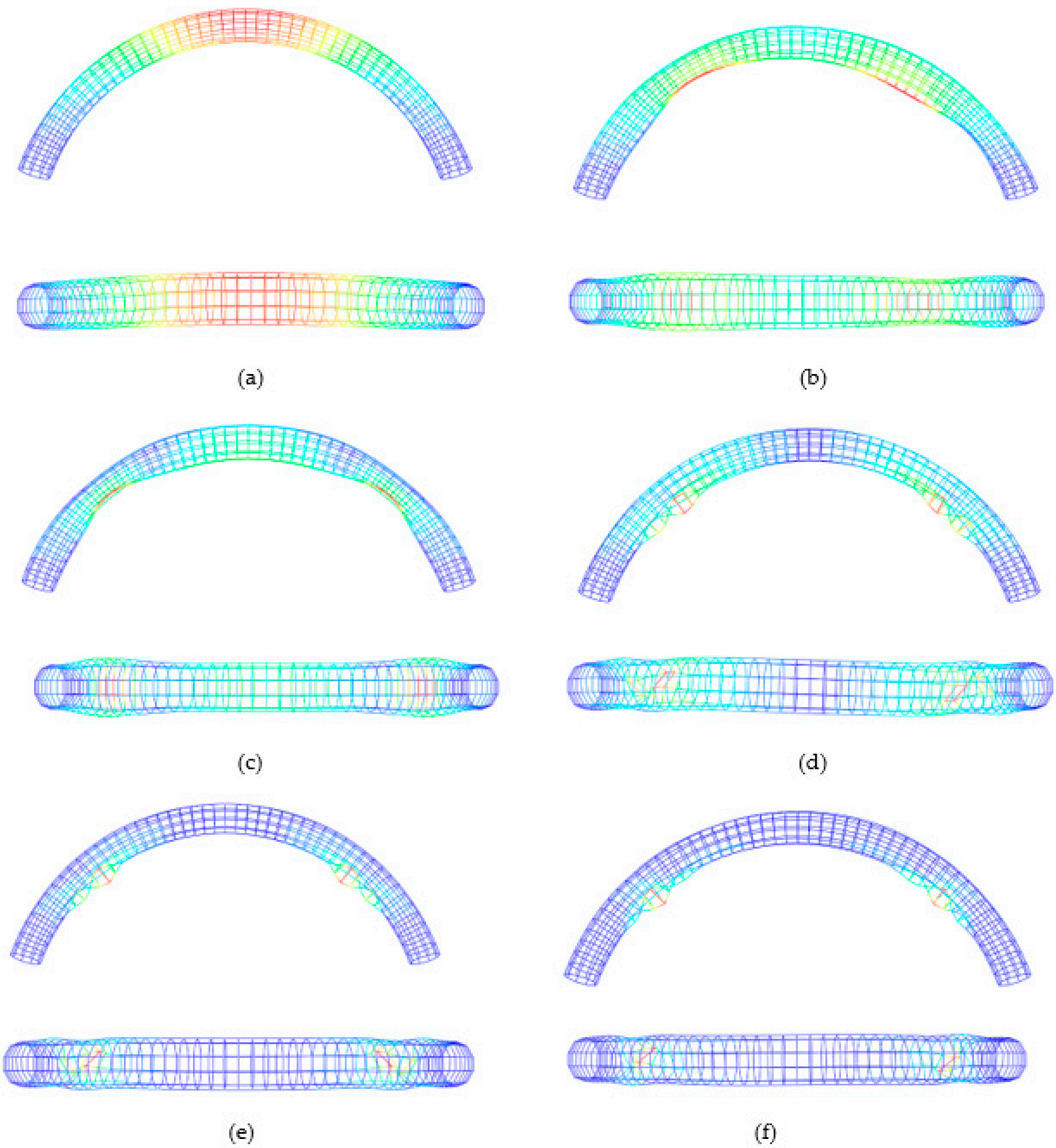

Figure 6. Buckling modes of the structure: (**a**) Mode 1; (**b**) Mode 2; (**c**) Mode 3; (**d**) Mode 4; (**e**) Mode 5; (**f**) Mode 6.

The elastic buckling loads for each mode are shown in Table 2.

Table 2. Summary of the linear buckling loads.

Modes	Mode 1	Mode 2	Mode 3	Mode 4	Mode 5	Mode 6
Linear buckling load factor *	56.57	75.75	82.89	83.76	84.03	84.19
Symmetry of deformation	symmetric	anti-symmetric	symmetric	anti-symmetric	symmetric	anti-symmetric

* Linear buckling load factor is the ratio of the elastic buckling load to the initial load (1.0Dead Load + 1.0Live Load).

In order to show the buckling mode more clearly, the deformation visualization scale factor was expanded to three times the original. In the first bucking mode, an overall lateral displacement out of the arch plane occurred, and the value of the lateral displacement decreased from the middle of the span to the feet of the arch. In the second bucking mode, the elliptical arch section of the left 1/4 span was compressed in the direction of the short axis, and the section of the right 1/4 span was elongated in the direction of the short axis. In the third bucking mode, the arch sections of both the left and right 1/4 span were compressed in the direction of the short axis, and the section at each foot of the arch was slightly bulged. In the fourth bucking mode, the grids at the left and right 1/4 span underwent large deformation. The fifth and sixth buckling modes were similar to the fourth, with larger grid deformation in the local area and change of deformation symmetry.

From the third buckling mode, the buckling load gradually became closer in value, and the buckling mode of the structure transited from the overall buckling to the buckling of the local region. In the third to sixth buckling mode, the location where buckling occurred was AREA5&6 of the structure. Compared with other regions, the ring component cross-section was BH-700 $\times$ 300 $\times$ 20 $\times$ 20, and the arch component cross-section was B.Pipe-600 $\times$ 26 in AREA5&6, both of which were the smallest in cross-sectional dimensions. At the same time, the maximum axial pressure occurred in these regions as Figure 7 shows, making them the most likely locations for buckling to occur.

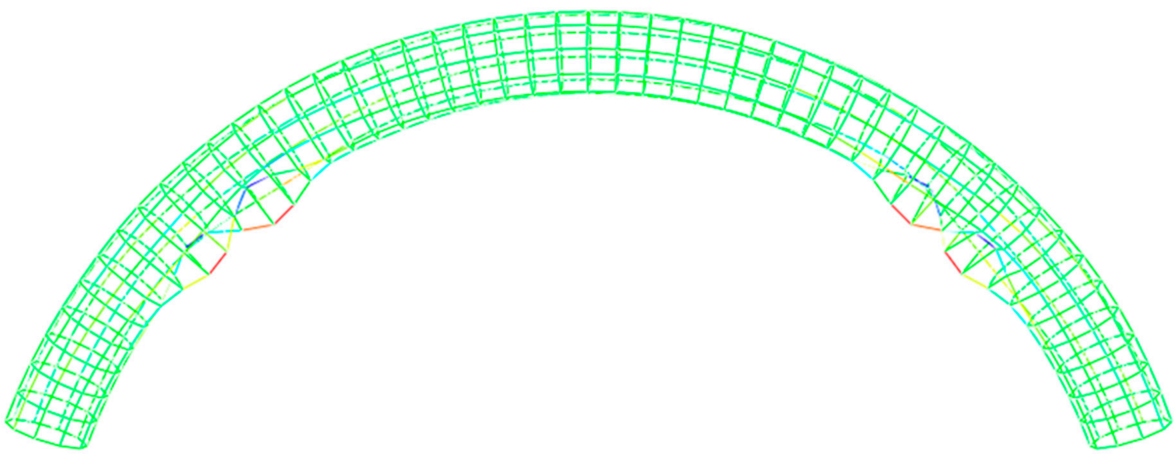

Figure 7. Axial force diagram of Mode 4.

3.2. Nonlinear Elasto-Plastic Stability Analysis

In order to analyze the ultimate load-bearing capacity of this structure more accurately, the initial geometric imperfections were introduced by the consistent mode imperfection method in the nonlinear elasto-plastic stability analysis. The initial geometric imperfection distribution was adopted from the first buckling mode of the structure, and the amplitude was taken as 1/300 of the span, respectively [35]. The full-range elasto-plastic analysis of the structure was carried out considering both geometric and material nonlinearities.

In the first buckling mode of linear buckling analysis, the point with maximum displacement was located in the middle of the structure, and the vertical displacement at this point was extracted as representative of the structural deflection in the elasto-plastic full-range analysis. The vertical axis was the load proportionality factor (LPF) of the structure, which is the ratio of the actual load to the initial load (1.0Dead Load + 1.0Live Load). The load-displacement curve of elasto-plastic full-range analysis is shown as Figure 8.

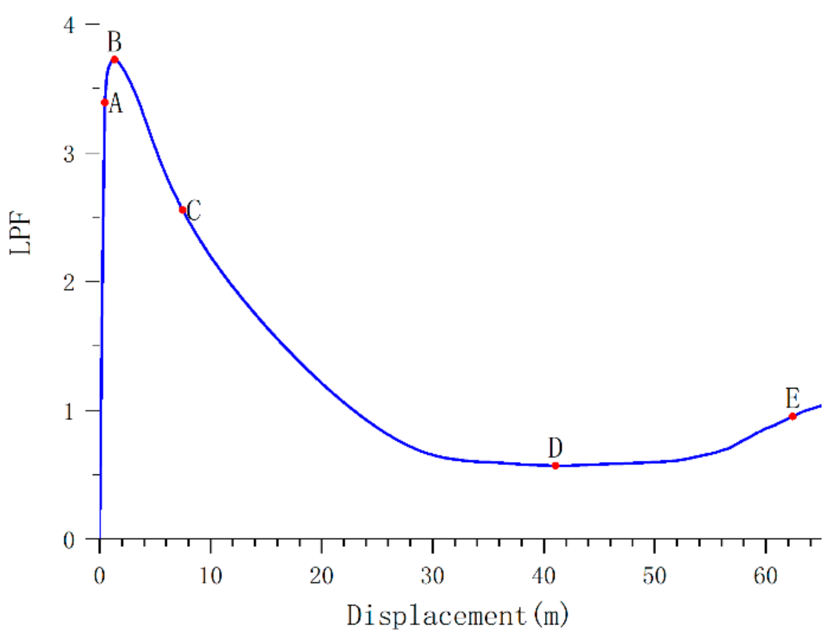

Figure 8. The load-displacement curve of elasto-plastic full-range analysis.

The stress distribution of the structure is shown in Figure 9. When the curve reached point A, the load reached 3.39 times the initial load (LPF = 3.39) and the vertical deflection of the structure was 0.479 m. The arch components in the upper part of the structure's middle section, the lower part of the 1/4 span section, and some at the feet of the structure, started to reach plasticity. As the load-displacement curve was linear, the overall structure was in the elastic stage in the stage O–A, and the structural stiffness was large.

Subsequently, the structure could still continue to carry the load, and the plastic range developed further with the increase in load, weakening the stiffness of the overall structure. The arch components and a few ring components at the middle and 1/4 span of the structure entered plasticity, and four more arch components at each foot of the structure reached plasticity. When the load reached 3.72 times the initial load, the structure reached the elasto-plastic ultimate load-bearing capacity and buckled, and the vertical deflection of the structure was 1.363 m. At this stage, most of the arch and ring components at the middle and 1/4 span of the structure reached plasticity, and all the arch components at the feet of the arch entered plasticity.

After buckling, the load decreased, with the displacement increasing rapidly, the structure as a whole was still in the compression and bending state, and the plastic range continued to increase, such as the stress and displacement pattern at point C. At this stage, most of the arch components reached plasticity, and the number of ring components that reached plasticity in the middle of the span, 1/4 span, and at the feet, continued to increase, and the plastic range became larger.

When the load continued to be applied, the vertical displacement of the structure increased rapidly. The structure as a whole gradually changed from compression and bending state, to tension and bending state. The tension edge of the structure reached the yield stress while the compression yield region gradually decreased, and the structure reached the reverse equilibrium state at point D. At this stage, the load was 0.57 times the initial load, and the structural deflection was 40.74 m. After point D, the bearing capacity of the structure was increasing. As the structure, as a whole, was in the tension and bending state, the compression yield region continued to decrease and the tensile yield region continued to increase, as shown in the Figure 9e. Although the simulation results show that the structure still has load carrying capacity, the state is no longer meaningful in engineering.

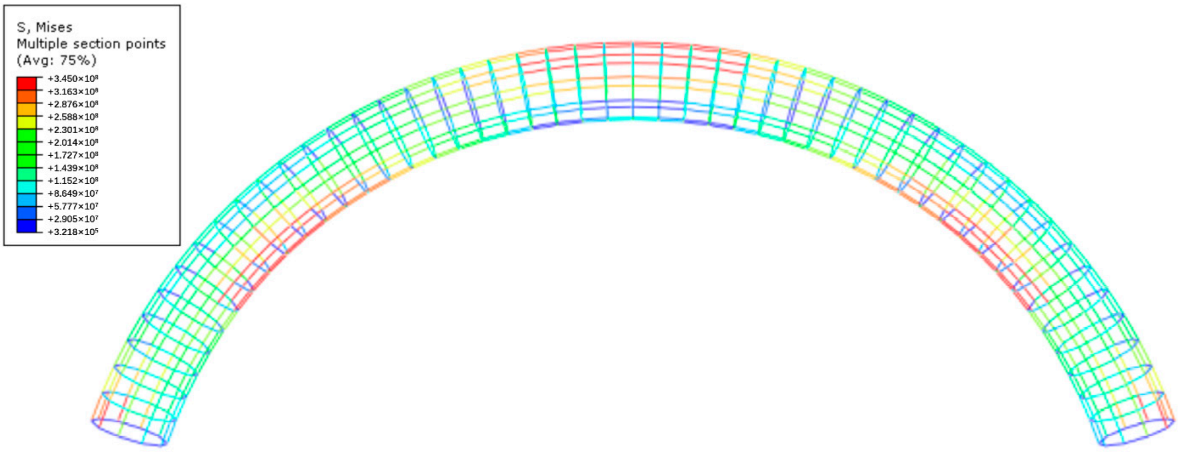

(**a**)

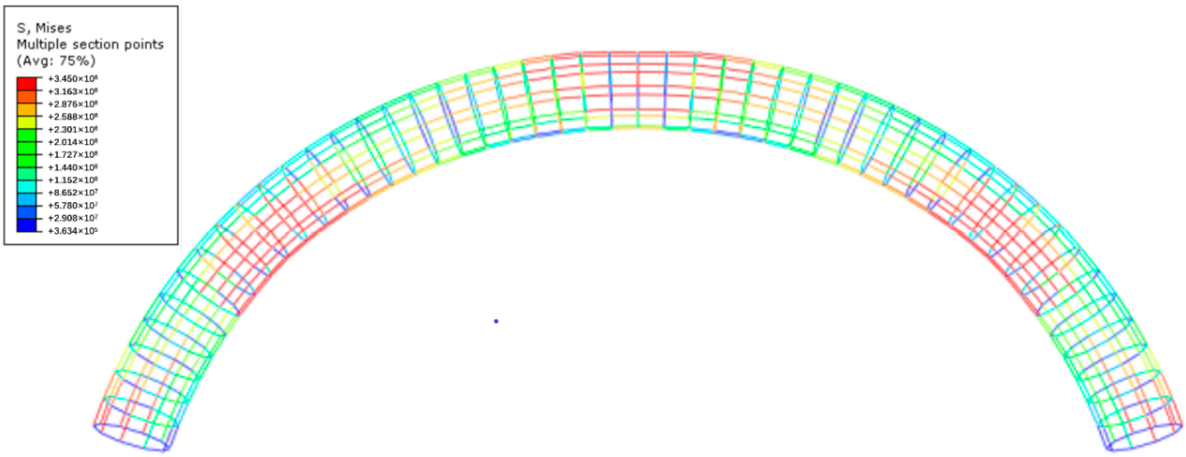

(**b**)

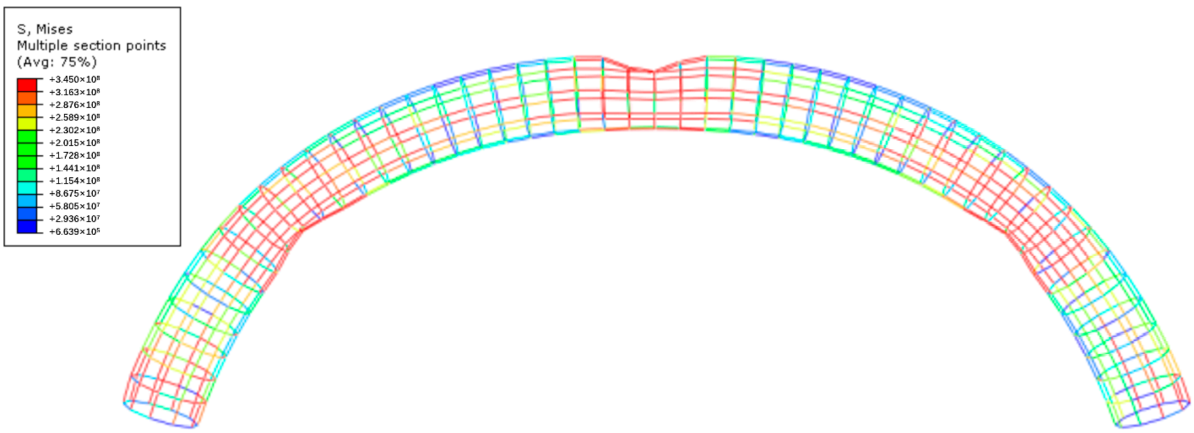

(**c**)

Figure 9. *Cont.*

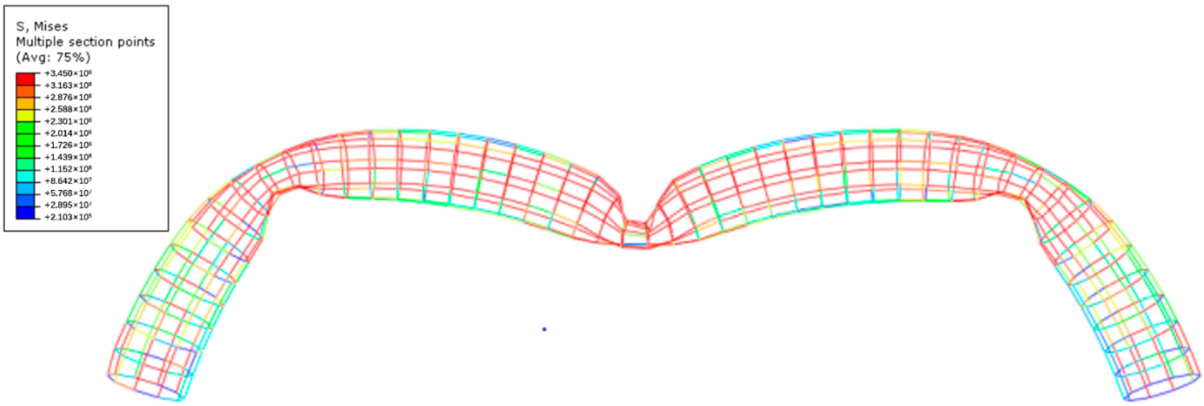

(**d**)

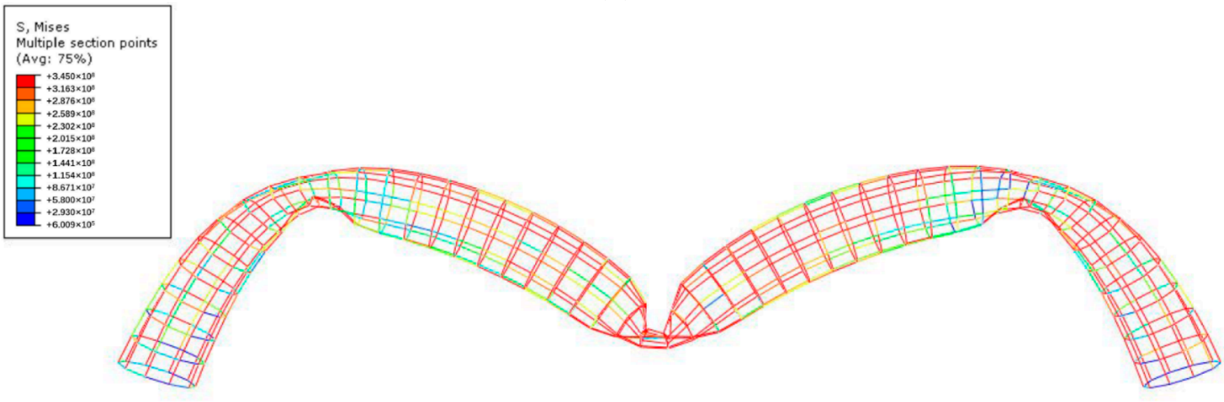

(**e**)

Figure 9. Stress distribution of the structure: (**a**–**e**) corresponds to the stage at point A–E in the load-displacement curve.

4. Analysis of the Factors Influencing Stability Bearing Capacity

4.1. Influence of Initial Geometric Imperfections

The actual engineering structure inevitably had various initial imperfections, including production and installation deviations and initial eccentricity of members to nodes, initial stresses caused by various reasons, etc. In order to study the influence of initial geometric imperfections on the structure's stability bearing capacity, four finite element models with initial geometric imperfection amplitudes of 1/100, 1/300, 1/500, and 1/1000 of the structure span, and one without geometric imperfection, were established. Both geometric nonlinearity and material nonlinearity were considered. The first buckling mode was chosen as the geometric initial imperfection distribution of the structure. Because the structural deformation pattern, according to this mode, was in the minimum potential energy state, there was a tendency for deformation along this mode at the initial load applying stage for the structure [35]. If the imperfection distribution of the structure was in the same form as the first buckling mode, it would have the most adverse effect on the structural load-bearing performance.

In the first buckling mode of linear buckling analysis, the point with maximum displacement was located in the middle of the structure, and the vertical displacement at this point was extracted as a representative of the structural deflection in the elasto-plastic full-range analysis. The vertical axis was the LPF of the structure. Figure 10 shows the load-displacement curves of full-range analysis with different initial imperfections.

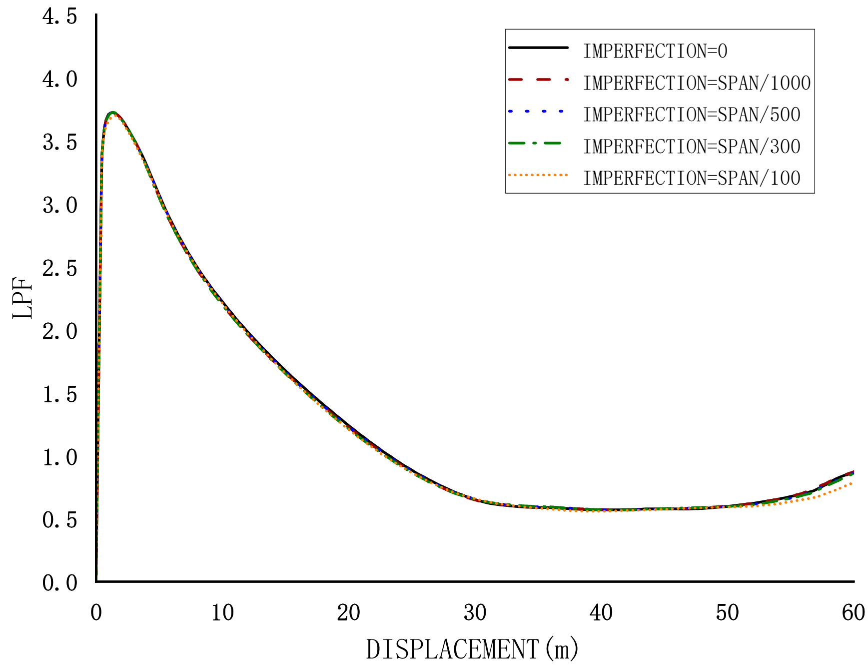

Figure 10. Load-displacement curves of full-range analysis with different initial imperfections.

It can be seen from Figure 10 that the load-displacement curves of the models with initial imperfections of 1/1000, 1/500 and 1/300 almost coincided with that of the model without imperfections. Only the ultimate load of the model with initial imperfections of 1/100 (LPF = 3.70) was slightly different from that of the model without imperfections (LPF = 3.72), while the imperfection maximum value reached 1.77 m, which is far beyond the actual construction-allowed range. It can be concluded that the construction error allowed in the project has a very small effect on the stability bearing capacity of the structure. At the same time, as the value of imperfection increases, the ultimate load-bearing capacity decreases, and deviations should be minimized during the construction of the structure.

4.2. Influence of Nonlinear Factors

In order to study the effects of material nonlinearity and geometric nonlinearity on the ultimate load-carrying capacity of the structure, the full-range analysis of the structure considering only geometric nonlinearity and only material nonlinearity was carried out separately and compared with the results of elasto-plastic stability analysis of the structure. The load-displacement curves of the structure are shown as Figure 11.

The load proportionality factor (LPF) gradually increased from 0 to point a (LPF = 3.39), during which the A, B and C curves coincide, illustrating that the structure is in the elastic stage.

The elastic stability behavior of the structure with large deformation can be obtained from load-displacement curve A, considering only the geometric nonlinearity, that the structure does not have an elastic ultimate load. By analyzing the stress and deformation of the structure, it was found that although the mid span area of the structure was most likely to buckle, the area was dominated by bending deformation. With the load increasing, the structure continued to bend downward, and its deformation mode and equilibrium mode remained unchanged. Therefore, it will continue to bear the load without buckling, and the cross-sectional stresses of the member in some areas have long exceeded the elastic limit.

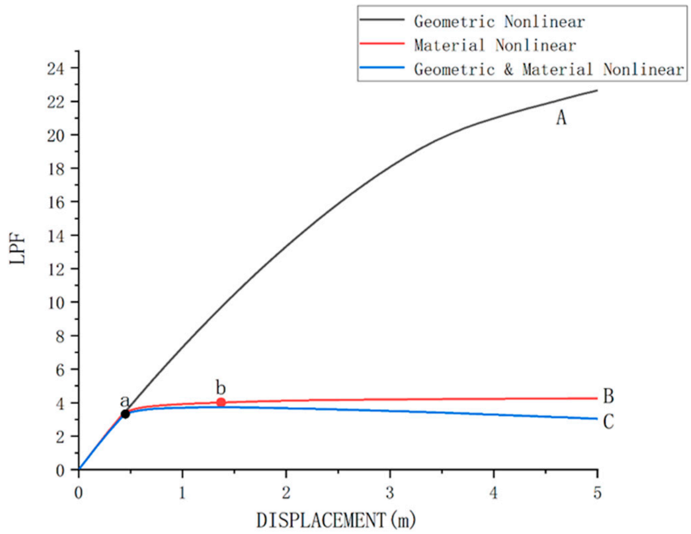

Figure 11. Load-displacement curves of full-range analysis with different nonlinear factors.

The elasto-plastic stability behavior of the structure with small deformation can be obtained from load-displacement curve B, considering only material nonlinearity, that the arch and ring components at the middle and 1/4 span, as well as the arch components at the feet, gradually reach plasticity with LPF increasing from 3.39 (point a) to 4.0 (point b). At this stage, the structural behavior is similar to the one considering both material nonlinearity and geometric nonlinearity, and curve B is slightly higher than curve C. The plasticity range gradually increases, and the LPF of curve B does not decrease. While the displacement keeps increasing, the load-displacement curve tends to be horizontal, and the behavior of the overall structure is nearly plastic at this stage. Since the geometric nonlinearity was not considered, the structure was still calculated according to the small deformation assumption, and its deformation mode did not change. Unlike the load-displacement curve C which considered both material nonlinearity and geometric nonlinearity, there is no descending portion in curve B.

The LPF corresponding to the ultimate load, considering only material nonlinearity, was 4.22, and the one considering material nonlinearity and geometric nonlinearity was 3.72. The influence of geometric nonlinearity on the ultimate bearing capacity of the structure was about 11.8%. The ultimate load-carrying capacity of the structure is sensitive to material nonlinearity, and a full-range analysis of the structure considering only geometric nonlinearity will seriously overestimate the ultimate load-carrying capacity of the structure, which would be unsafe for the engineering project. In summary, to evaluate the ultimate load-carrying capacity of the structure, both material nonlinearity and geometric nonlinearity should be considered.

5. Conclusions

In this paper, the elastic and elasto-plastic stability behavior considering the initial geometric imperfections of the large-span spatial grid arch structure based on Eye of the Yellow Sea project were analyzed, and the buckling mode as well as the full-range load-displacement curve of the structure were obtained. The full-range stress distribution, deformation mode and overall performance of the structure were studied. The influence of initial geometric imperfections and nonlinearities on the structural ultimate load-carrying capacity were investigated. The following main conclusions were obtained:

(1) In the first bucking mode, an overall out-of-plane lateral displacement occurred in the middle area of the span. The locations of maximum stress and deformation of the bucking modes 2~6 were at the left and right 1/4 span of the structure. The linear buckling load became progressively closer from bucking mode three, and the locations where buckling occurred were located in the 1/4 span local area, where

the component cross-sectional dimensions were the smallest. The maximum axial pressure occurred in these areas, making them the most likely locations for buckling to occur;

(2) The full-range analysis considering geometric nonlinearity, material nonlinearity and initial imperfections showed that with the change of load, the structure went through the elastic stage, plastic development stage, the stage of buckling when the ultimate load was reached, the stage of displacement increasing rapidly while the load-carrying capacity was decreasing rapidly, and the stage of reverse equilibrium;

(3) When the initial geometric imperfection amplitude was set as 1/1000, 1/500, and 1/300 of the span, the stability behavior of the structure was almost unaffected. Only when the initial imperfection was 1/100 of the span, the ultimate load of the structure was reduced by 0.54%;

(4) The influence of geometric nonlinearity on the ultimate bearing capacity of the structure was 11.8%;

(5) The ultimate load-carrying capacity of the structure is sensitive to material nonlinearity. Considering only geometric nonlinearity will seriously overestimate the ultimate bearing capacity of the structure, which would be unsafe for the project. To evaluate the ultimate load-carrying capacity of the structure, both material nonlinearity and geometric nonlinearity should be considered.

Author Contributions: Conceptualization, Z.C. and X.W.; methodology, Z.C., X.W., H.L. (Hongbo Liu) and H.L. (Hao Lin); software, H.L. (Hao Lin); formal analysis, H.L. (Hao Lin); validation, H.L. (Hao Lin), K.K. and M.M.; investigation, H.L. (Hao Lin), K.K. and M.M.; writing—original draft preparation, H.L. (Hao Lin); writing—review and editing, Z.C., X.W., H.L. (Hongbo Liu) and H.L. (Hao Lin); project administration, Z.C. and X.W.; funding acquisition, H.L. (Hongbo Liu). All authors have read and agreed to the published version of the manuscript.

Funding: This research was funded by Hebei Province Full-time Top-level Talents Introduction Project, grant number [2020HBQZYC013].

Institutional Review Board Statement: Not applicable.

Informed Consent Statement: Not applicable.

Data Availability Statement: Not applicable.

Acknowledgments: Special thanks to the Institute of Steel Structures, Department of Civil Engineering, Tianjin University, for the help and support.

Conflicts of Interest: The authors declare no conflict of interest.

References

1. Timoshenko, S.P.; Gere, J.M. *Theory of Elastic Stability*, 2nd ed.; Dover Publications, Inc.: New York, NY, USA, 2009; pp. 297–302.
2. Pi, Y.L.; Bradford, M.A.; Uy, B. In-Plane Stability of Arches. *Int. J. Solids Struct.* **2002**, *39*, 105–125. [CrossRef]
3. Bradford, M.A.; Uy, B.; Pi, Y.-L. In-Plane Elastic Stability of Arches under a Central Concentrated Load. *J. Eng. Mech.* **2002**, *128*, 710–719.
4. Pi, Y.L.; Bradford, M.A.; Tin-Loi, F. Nonlinear Analysis and Buckling of Elastically Supported Circular Shallow Arches. *Int. J. Solids Struct.* **2007**, *44*, 2401–2425. [CrossRef]
5. Pi, Y.L.; Bradford, M.A.; Tin-Loi, F. Non-Linear in-Plane Buckling of Rotationally Restrained Shallow Arches under a Central Concentrated Load. *Int. J. Non-Linear Mech.* **2008**, *43*, 1–17. [CrossRef]
6. Pi, Y.L.; Bradford, M.A. Non-Linear in-Plane Postbuckling of Arches with Rotational End Restraints under Uniform Radial Loading. *Int. J. Non-Linear Mech.* **2009**, *44*, 975–989. [CrossRef]
7. Pi, Y.L.; Bradford, M.A. Non-Linear in-Plane Analysis and Buckling of Pinned-Fixed Shallow Arches Subjected to a Central Concentrated Load. *Int. J. Non-Linear Mech.* **2012**, *47*, 118–131. [CrossRef]
8. Pi, Y.L.; Bradford, M.A. Nonlinear Elastic Analysis and Buckling of Pinned-Fixed Arches. *Int. J. Mech. Sci.* **2013**, *68*, 212–223. [CrossRef]
9. Pi, Y.L.; Bradford, M.A. Nonlinear Analysis and Buckling of Shallow Arches with Unequal Rotational End Restraints. *Eng. Struct.* **2013**, *46*, 615–630. [CrossRef]
10. Hodges, D.H. Non-linear inplane deformation and buckling of rings and high arches. *Int. J. Non-Linear Mech.* **1999**, *34*, 723–737. [CrossRef]

11. Sakimoto, T.; Namita, Y. Out-Of-Plane Buckling of Solid Rib Arches Braced with Transverse Bars. *Proc. Jpn. Soc. Civ. Eng.* **1971**, *191*, 109–116. [CrossRef]
12. Pi, Y.L.; Bradford, M.A. Elastic flexural–torsional buckling of fixed arches. *Q. J. Mech. Appl. Math.* **2004**, *57*, 551–569. [CrossRef]
13. Pi, Y.L.; Bradford, M.A. Effects of Prebuckling Deformations on the Elastic Flexural-Torsional Buckling of Laterally Fixed Arches. *Int. J. Mech. Sci.* **2004**, *46*, 321–342. [CrossRef]
14. Pi, Y.L.; Bradford, M.A.; Trahair, N.S.; Chen, Y.Y. A further study of flexural-torsional buckling of elastic arches. *Int. J. Struct. Stab. Dyn.* **2005**, *5*, 163–183. [CrossRef]
15. Pi, Y.L.; Bradford, M.A.; Chen, Y.Y. An equilibrium approach for flexural-torsional buckling of elastic arches. *Adv. Steel Constr.* **2005**, *1*, 47–66.
16. Bradford, M.A.; Pi, Y.L. Flexural-Torsional Buckling of Fixed Steel Arches under Uniform Bending. *Proc. J. Constr. Steel Res.* **2006**, *62*, 20–26. [CrossRef]
17. Bradford, M.A.; Pi, Y.L. Elastic Flexural-Torsional Buckling of Circular Arches under Uniform Compression and Effects of Load Height. *J. Mech. Mater. Struct.* **2006**, *1*, 1235–1255. [CrossRef]
18. Pi, Y.L.; Bradford, M.A.; Tin-Loi, F. Flexural-Torsional Buckling of Shallow Arches with Open Thin-Walled Section under Uniform Radial Loads. *Thin-Walled Struct.* **2007**, *45*, 352–362. [CrossRef]
19. Bradford, M.A.; Pi, Y.L. Elastic Flexural-Torsional Instability of Structural Arches under Hydrostatic Pressure. *Int. J. Mech. Sci.* **2008**, *50*, 143–151. [CrossRef]
20. Pi, Y.L.; Bradford, M.A.; Tong, G.S. Elastic Lateral-Torsional Buckling of Circular Arches Subjected to a Central Concentrated Load. *Int. J. Mech. Sci.* **2010**, *52*, 847–862. [CrossRef]
21. Bradford, M.A.; Pi, Y.L. A New Analytical Solution for Lateral-Torsional Buckling of Arches under Axial Uniform Compression. *Eng. Struct.* **2012**, *41*, 14–23. [CrossRef]
22. Pi, Y.L.; Bradford, M.A. Lateral-Torsional Elastic Buckling of Rotationally Restrained Arches with a Thin-Walled Section under a Central Concentrated Load. *Thin-Walled Struct.* **2013**, *73*, 18–26. [CrossRef]
23. Pi, Y.L.; Bradford, M.A. Lateral-Torsional Buckling Analysis of Arches Having In-Plane Rotational End Restraints under Uniform Radial Loading. *J. Eng. Mech.* **2013**, *139*, 1602–1609. [CrossRef]
24. Dou, C.; Guo, Y.L.; Zhao, S.Y.; Pi, Y.L.; Bradford, M.A. Elastic Out-of-Plane Buckling Load of Circular Steel Tubular Truss Arches Incorporating Shearing Effects. *Eng. Struct.* **2013**, *52*, 697–706. [CrossRef]
25. Guo, Y.-L.; Zhao, S.-Y.; Bradford, M.A.; Pi, Y.-L. Threshold Stiffness of Discrete Lateral Bracing for Out-of-Plane Buckling of Steel Arches. *J. Struct. Eng.* **2015**, *141*, 04015004. [CrossRef]
26. Guo, Y.L.; Zhao, S.Y.; Dou, C. Out-of-Plane Elastic Buckling Behavior of Hinged Planar Truss Arch with Lateral Bracings. *J. Constr. Steel Res.* **2014**, *95*, 290–299. [CrossRef]
27. Komatsu, S.; Sakimoto, T. Ultimate Load Carrying Capacity of Steel Arches. *J. Struct. Div.* **1977**, *103*, 2323–2336. [CrossRef]
28. Sakimoto, T.; Komatsu, S. Ultimate Strength Formula for Steel Arches. *J. Struct. Eng.* **1983**, *109*, 613–627. [CrossRef]
29. Pi, Y.L.; Trahair, N.S. Out-of-Plane Inelastic Buckling and Strength of Steel Arches. *J. Struct. Eng.* **1998**, *124*, 174–183. [CrossRef]
30. Pi, Y.L.; Trahair, N.S. Inelastic lateral buckling strength and design of steel arches. *Eng. Struct.* **2000**, *22*, 993–1005. [CrossRef]
31. Pi, Y.L.; Bradford, M.A. Out-of-Plane Strength Design of Fixed Steel I-Section Arches. *J. Struct. Eng.* **2005**, *131*, 560–568. [CrossRef]
32. Dou, C.; Guo, Y.-L.; Pi, Y.-L.; Zhao, S.-Y. Flexural-Torsional Buckling and Ultimate Resistance of Parabolic Steel Arches Subjected to Uniformly Distributed Vertical Load. *J. Struct. Eng.* **2014**, *140*, 04014075. [CrossRef]
33. Dou, C.; Guo, Y.-L.; Zhao, S.-Y.; Pi, Y.-L. Experimental Investigation into Flexural-Torsional Ultimate Resistance of Steel Circular Arches. *J. Struct. Eng.* **2015**, *141*, 04015006. [CrossRef]
34. Chen, Z.; Xu, H.; Zhao, Z.; Yan, X.; Zhao, B. Investigations on the Mechanical Behavior of Suspend-Dome with Semirigid Joints. *J. Constr. Steel Res.* **2016**, *122*, 14–24. [CrossRef]
35. Liu, H.; Ding, Y.; Chen, Z. Static Stability Behavior of Aluminum Alloy Single-Layer Spherical Latticed Shell Structure with Temcor Joints. *Thin-Walled Struct.* **2017**, *120*, 355–365. [CrossRef]